



Angus, D. A., Fisher, Q. J., Segura, J. M., Verdon, J. P., Kendall, J. M., Dutko, M., & Crook, A. J. L. (2016). Reservoir stress path and induced seismic anisotropy: results from linking coupled fluid-flow/geomechanical simulation with seismic modelling. *Petroleum Science*, 13(4), 669-684. <https://doi.org/10.1007/s12182-016-0126-1>

Publisher's PDF, also known as Version of record

License (if available):  
CC BY

Link to published version (if available):  
[10.1007/s12182-016-0126-1](https://doi.org/10.1007/s12182-016-0126-1)

[Link to publication record in Explore Bristol Research](#)  
PDF-document

This is the final published version of the article (version of record). It first appeared online via Springer at [https://doi.org/ 10.1007/s12182-016-0126-1](https://doi.org/10.1007/s12182-016-0126-1) . Please refer to any applicable terms of use of the publisher.

## University of Bristol - Explore Bristol Research

### General rights

This document is made available in accordance with publisher policies. Please cite only the published version using the reference above. Full terms of use are available:  
<http://www.bristol.ac.uk/red/research-policy/pure/user-guides/ebr-terms/>

# Reservoir stress path and induced seismic anisotropy: results from linking coupled fluid-flow/geomechanical simulation with seismic modelling

D. A. Angus<sup>1,7</sup> · Q. J. Fisher<sup>1</sup> · J. M. Segura<sup>2,6</sup> ·  
J. P. Verdon<sup>3</sup> · J.-M. Kendall<sup>3</sup> · M. Dutko<sup>4</sup> ·  
A. J. L. Crook<sup>5</sup>

Received: 21 October 2015 / Published online: 1 November 2016  
© The Author(s) 2016. This article is published with open access at Springerlink.com

**Abstract** We present a workflow linking coupled fluid-flow and geomechanical simulation with seismic modelling to predict seismic anisotropy induced by non-hydrostatic stress changes. We generate seismic models from coupled simulations to examine the relationship between reservoir geometry, stress path and seismic anisotropy. The results indicate that geometry influences the evolution of stress, which leads to stress-induced seismic anisotropy. Although stress anisotropy is high for the small reservoir, the effect of stress arching and the ability of the side-burden to support the excess load limit the overall change in effective stress and hence seismic anisotropy. For the extensive reservoir, stress anisotropy and induced seismic anisotropy are high. The extensive and elongate reservoirs experience significant compaction, where the inefficiency of the developed stress arching in the side-burden cannot support the excess load. The elongate reservoir displays significant stress asymmetry, with seismic anisotropy developing predominantly along the long-edge of the reservoir. We show that the link between

stress path parameters and seismic anisotropy is complex, where the anisotropic symmetry is controlled not only by model geometry but also the nonlinear rock physics model used. Nevertheless, a workflow has been developed to model seismic anisotropy induced by non-hydrostatic stress changes, allowing field observations of anisotropy to be linked with geomechanical models.

**Keywords** Coupled fluid-flow/geomechanics · Reservoir characterization · Seismic anisotropy · Stress path

## 1 Introduction

Extraction and injection of fluids within hydrocarbon reservoirs alters the in situ pore pressure leading to changes in the effective stress field within the reservoir and surrounding rocks. However, changes in pore pressure do not necessarily lead to a hydrostatic change in effective stress. For instance, a reduction in fluid pressure within a reservoir is often accompanied by a slower increase in the minimum effective horizontal stress with respect to the vertical effective stress change (e.g., Segura et al. 2011). This asymmetry can result in the development of stress anisotropy that may promote elastic failure within the rock, such as fault reactivation and borehole deformation. From the perspective of seismic monitoring, changes in the stress field can lead to microseismicity as well as nonlinear changes in seismic velocity and, in cases where stress anisotropy develop, to stress-induced seismic anisotropy. This has important implications on the interpretation of time-lapse (4D) seismic as well as microseismic data, where stress anisotropy can result in anisotropic perturbations in the velocity field, offset and azimuthal variations in reflection amplitudes and shear-wave splitting.

✉ D. A. Angus  
D.Angus@leeds.ac.uk

<sup>1</sup> School of Earth and Environment, University of Leeds, Leeds, UK

<sup>2</sup> Formerly School of Earth and Environment, University of Leeds, Leeds, UK

<sup>3</sup> Department of Earth Sciences, University of Bristol, Bristol, UK

<sup>4</sup> Rockfield Software Ltd., Swansea, UK

<sup>5</sup> Three Cliffs Geomechanics, Swansea, UK

<sup>6</sup> Present Address: Repsol, Madrid, Spain

<sup>7</sup> Present Address: ESG Solutions, Kingston, Canada

Reservoir stress path, expressed as the ratio of change of effective horizontal to effective vertical stress from an initial stress state, is a useful concept in characterizing the evolution of stress anisotropy due to production (e.g., Aziz and Settari 1979; Sayers 2007; Alassi et al. 2010). The stress path of a reservoir during production is sensitive to the geometry of the reservoir system, pore pressure and the material properties of the reservoir and surrounding rock mass (e.g., Segura et al. 2011). In the field, stress path can be measured from borehole pressure tests, and so maps of reservoir stress path are extrapolated out into the reservoir via limited discrete measurements. History matching borehole reservoir stress path parameters with seismic anisotropy measurements may provide a more reliable prediction of reservoir stress path throughout the reservoir volume. However, linking seismic anisotropy measurements with stress path requires a better understanding of the link between geomechanical deformation (evolution of stress and strain), fluid-flow, rock physical properties and seismic attributes.

Recent studies focusing on linking numerical coupled fluid-flow and geomechanical simulation with seismic modelling have improved our understanding of the relationship between seismic attributes, fluid properties and mechanical deformation due to reservoir fluid extraction and injection (e.g., Rutqvist et al. 2002; Dean et al. 2003; Herwanger and Horne 2009; Alassi et al. 2010; Herwanger et al. 2010; Verdon et al. 2011; He et al. 2015; Angus et al. 2015). Analytic and semi-analytic approaches using poroelastic formulations have previously been used to understand surface subsidence (e.g., Geertsma 1973) and seismic travel-time shifts (e.g., Fuck et al. 2009; Fuck et al. 2010) due to pore pressure changes. Coupled fluid-flow and geomechanical numerical simulation algorithms integrate the influence of multi-phase fluid-flow as well as deviatoric stress and strain to provide more accurate models of the spatial and temporal behaviour of various rock properties within and outside the reservoir (e.g., Herwanger et al. 2010). Linking changes in reservoir physical properties, such as porosity, permeability and bulk modulus, to changes in seismic attributes is accomplished via rock physics models (e.g., Prioul et al. 2004) to generate so-called dynamic (high strain rate and low strain magnitude suitable for seismic frequencies) elastic models.

In this paper, we investigate the sensitivity of seismic anisotropy to reservoir stress path using the micro-structural nonlinear rock physics model of Verdon et al. (2008). This work follows the coupled fluid-flow and geomechanical characterization of reservoir stress path of Segura et al. (2011), who explore the influence of reservoir geometry and material property contrast on stress path for poroelastic media. We present results from coupled fluid-flow and geomechanical simulations for the same

geometries to investigate stress-induced seismic anisotropy. A major point of departure of our approach to the approaches of Rutqvist et al. (2002), Herwanger and Horne (2009) and Fuck et al. (2009) is that we extend the material behaviour from poroelastic to include plasticity (i.e., so-called poroelastoplastic behaviour). Poroelastoplasticity can incorporate matrix failure during simulation, allowing strain hardening and weakening to develop within the model. This is especially important for modelling reservoir stress path and stress path asymmetry. Furthermore, poroelastoplasticity also enables the prediction of when and where failure occurs in the model, allowing us to model the likely microseismic response of a reservoir (Angus et al. 2010, 2015).

## 2 Modelling approach

### 2.1 Coupled fluid-flow and geomechanical simulation

Industry-standard fluid-flow simulation algorithms solve the equations of flow for multi-phase fluids (e.g., Aziz and Settari 1979), but neglect the influence of changing pore pressure on the geomechanical behaviour of the reservoir and surrounding rock. Formulations exist for fully coupled fluid-flow and geomechanical simulation, yet they tend to be computationally expensive (e.g., Minkoff et al. 2003). However, iterative and loose coupling of fluid-flow simulators with geomechanical solvers can be more efficient and yield sufficiently accurate results compare to fully coupled solutions (e.g., Dean et al. 2003; Minkoff et al. 2003). Furthermore, iterative and loosely coupled approaches allow the use of already existing commercial reservoir fluid-flow modelling software. In this paper, the coupled fluid-flow and geomechanical simulations are performed using the finite-element geomechanical solver ELFEN (Rockfield Software Ltd.) linked with the commercial fluid-flow simulation package TEMPEST (Roxar), where the simulations are loosely coupled using a message-passing interface (Muntz et al. 2007).

Predicting the geomechanical response of reservoirs depends on the ability of the geomechanical solver to model the nonlinear behaviour of rocks. The nonlinear dependence of rocks with stress is generally attributed to closure of microcracks and pores, as well as increasing grain boundary contact with increasing confining stress (e.g., Nur and Simmons 1969). Rocks also display stress hysteresis (e.g., Helbig and Rasolofosaon 2000), and this hysteresis has been observed to occur not only at large strains but also small strains (e.g., Johnson and Rasolofosaon 1996). This observation represents a potentially important rock characteristic in explaining the asymmetric

behaviour of 4D seismic observations of producing reservoirs (e.g., Hatchell and Bourne 2005). Thus, it is important to incorporate such nonlinear and hysteretic properties within a constitutive model for coupled flow-geomechanical simulation. The constitutive relationships used by ELFEN are derived from laboratory experiments that incorporate linear elastic and plastic behaviour (e.g., Crook et al. 2002) as well as lithology specific behaviour (e.g., Crook et al. 2006). Specifically, the constitutive model used for the simulations within this paper is the so-called SR3 model. This model is defined as a single-surface rate-independent non-associated elastoplastic model that includes geomechanical anisotropy, rate dependence and creep into the basic material characterization (e.g., Crook et al. 2006). In other words, the constitutive model can include the effects of both linear elastic and nonlinear static elastoplastic response.

## 2.2 Micro-structural nonlinear rock physics model

To model the seismic response due to geomechanical deformation, rock physics model is required to link changes in fluid saturation, pore pressure and triaxial stresses to changes in the dynamic elastic stiffness. Rock physics models should incorporate phenomena observed in both laboratory core experiments and in the field, such as the nonlinear stress-velocity response (e.g., Nur and Simmons 1969; Sayers 2007; Hatchell and Bourne 2005) and the development of stress-induced anisotropy in initially isotropic rocks (e.g., Dewhurst and Siggins 2006; Olofsson et al. 2003).

The model we have developed is based on the approach outlined by Sayers and Kachanov (1995) and Schoenberg and Sayers (1995), where the overall compliance of the rock  $S_{ijkl}$  (compliance being the inverse of stiffness) is a function of the background compliance of the rock frame,  $S_{ijkl}^0$ , plus additional compliance introduced by the presence of low aspect ratio, highly compliant pore space  $\Delta S_{ijkl}$  (such as microcracks or grain boundaries),

$$S_{ijkl} = S_{ijkl}^0 + \Delta S_{ijkl}. \quad (1)$$

$S_{ijkl}^0$  can be estimated from either the mineral composition (e.g., Kendall et al. 2007) or the behaviour at high effective stresses, where it is assumed that the compliant pore space is completely closed (e.g., Sayers 2002). The additional compliance can be modelled using second- and fourth-rank crack density tensors  $\alpha_{ij}$  and  $\beta_{ijkl}$ , respectively,

$$\Delta S_{ijkl} = \frac{1}{4}(\delta_{ik}\alpha_{jl} + \delta_{il}\alpha_{jk} + \delta_{jk}\alpha_{il} + \delta_{jl}\alpha_{ik}) + \beta_{ijkl}. \quad (2)$$

Sayers (2002), Hall et al. (2008) and Verdon et al. (2008) apply this micro-structural formulation to invert for stress-dependent elastic stiffness and observe that the

behaviour of sedimentary rock can be modelled adequately using the second-rank crack density tensor  $\alpha_{ij}$  and assuming the fourth-rank crack density tensor  $\beta_{ijkl}$  is negligible.

Based on this micro-structural approach, Verdon et al. (2008) incorporate the analytical formulation of Tod (2002) to predict the response of the crack density tensor to changes in effective stress. The crack number density (hereafter referred to as crack density) for each diagonal component of  $\alpha_{ij}$  is expressed as a function of the initial crack density at a reference stress state,  $\varepsilon_i^0$ , and the average initial crack aspect ratio,  $a_i^0$ , at this reference stress state.

$$\alpha_{ii} = \frac{\varepsilon_i^0}{h_i} e^{(-c_r \sigma_{ii}^e)}, \quad (3)$$

where

$$c_r = \frac{\lambda_i + 2\mu_i}{(\pi\mu_i a_i^0)(\lambda_i + \mu_i)} \text{ and } h_i = \frac{3E_i(2 - \nu_i)}{32(1 - \nu_i^2)} \quad (4)$$

$E_i$  is Young's modulus,  $\nu_i$  is Poisson's ratio, and  $\lambda_i$  and  $\mu_i$  are the Lamé constants of the background material.  $\sigma_{ii}^e$  is the principal effective stress in the  $i$ th direction. This derivation yields an expression for the dynamic elastic stiffness that models stress-dependent seismic velocities and seismic anisotropy induced by non-hydrostatic stress fields.

The nonlinear rock physics model is incorporated within an aggregate elastic model (see Angus et al. 2011). The approach has the benefit of allowing us to incorporate the many causes of seismic anisotropy that act on multiple length-scales. Intrinsic anisotropy, caused by alignment of anisotropic mineral crystals (such as clays and micas), is included using an anisotropic background elasticity  $S_{ijkl}^0$ . Stress-induced anisotropy is incorporated implicitly within our rock physics model. For instance, even if initial crack density terms are isotropic ( $\varepsilon_1^0 = \varepsilon_2^0 = \varepsilon_3^0$ ), the second-order crack density terms are anisotropic ( $\alpha_{11} \neq \alpha_{22} \neq \alpha_{33}$ ) unless the stress field is hydrostatic. Finally, the influence of larger-scale fracture sets can also be modelled using the Schoenberg and Sayers (1995) effective medium approach, adding the additional compliance of the larger fracture sets to the stress-sensitive compliance computed in Eq. (6). Fluid substitution can also be included into this rock physics model, using either the Brown and Korrington (1975) anisotropic extension to Gassmann's equation, which is appropriate as a low-frequency end member, or incorporating the dispersive effects of squirt flow between pores (e.g., Chapman 2003). In this paper, we focus on the development of stress-induced anisotropy, assuming that the rock has no intrinsic anisotropy, and that large-scale fracture sets are not present. Although squirt flow has been shown to generate observable seismic anisotropy (e.g., Maultzsch et al. 2003; Baird et al. 2013), in this paper, we focus on the influence of

stress on seismic anisotropy and so ignore fluid substitution and squirt-flow effects.

The necessary input parameters for the nonlinear analytical model are the background elasticity ( $C_{ijkl}^0 = 1/S_{ijkl}^0$ ), effective triaxial stress tensor ( $\sigma_{ijkl}^e$ ), and the initial crack density and aspect ratio ( $\varepsilon_i^0$  and  $a_i^0$ ). Populating dynamic stress-dependent elastic models from the coupled flow-geomechanical simulation are achieved by passing the background static elastic tensor, rock density, stress tensor and pore pressure for each grid point within the model. The static stiffness is often observed empirically to correlate with dynamic stiffness (e.g., Olsen et al. 2008), providing a potential starting point for seismic modelling when independent estimates of the initial, pre-production seismic velocities are not available. Because we have no independent seismic information for these idealized models, we assume that the initial dynamic stiffness is scaled to the static stiffness. Additionally, there are parameters needed for the rock physics model that are not provided by the geomechanical simulation, in particular the initial crack density and aspect ratio. These parameters are derived from stress-velocity behaviour observed in core samples. Angus et al. (2009, 2012) provide a catalogue of over 200 of such measurements for a range of lithologies, inverting for  $\varepsilon^0$  and  $a^0$  to provide constraints for typical values of these parameters.

Before performing the coupled flow-geomechanical simulations, a geomechanical equilibration stage is required for all model geometries. Specifically, the stress state within the models evolves from an initial equilibrium state where the horizontal effective stresses are defined as a function of the vertical effective stress using horizontal stress coefficients. Thus, the initial stress field is non-hydrostatic and controlled by the reservoir geometry, model material properties and initial depth-dependent pore pressure. Application of the analytic stress-dependent rock physics model (Eqs. 1–3) would lead to initially anisotropic elasticity due to the non-hydrostatic effective stresses. To focus solely on the development of stress-dependent anisotropy related to production-induced changes in effective stresses, we include a stress initiation term  $\Delta S_{ijkl}^{\text{init}}$  in Eq. (1), to ensure that the initial overall compliance  $S_{ijkl}$  is isotropic and scaled to the inverse of the static geomechanical elastic stiffness:

$$S_{ijkl} = S_{ijkl}^0 + \Delta S_{ijkl} - \Delta S_{ijkl}^{\text{init}}, \quad (5)$$

where the stress initialization second-rank crack density term is defined

$$\alpha_{ii}^{\text{init}} = \frac{\varepsilon_i^0}{h_i} e^{-c_i \sigma_{ii}^{\text{init}}} \quad (6)$$

and  $\sigma_{ii}^{\text{init}}$  is the initial (baseline) principal effective stress in the  $i$ th direction. Including the stress initiation term

prescribes an initially isotropic elastic tensor equal to the static elastic tensor provided from the geomechanical solver. However, there is flexibility to incorporate various forms of anisotropy, which can be due to sedimentary and/or tectonic fabric (e.g., fine layering and fractures) as well as a basin and/or regionally developed stress related anisotropy (e.g., stress disequilibrium related to basin uplift) by adding additional anisotropic compliance terms. It should be noted that we use the static elasticity to compute the seismic velocities, and hence the magnitude of the seismic velocities is lower than typically observed in the field. Given that we are considering simple models, we choose not to perform a static-to-dynamic elasticity conversion (e.g., Angus et al. 2011) as would typically be done for field studies (e.g., He et al. 2016a). As this would involve a constant shift, not performing a static-to-dynamic elasticity conversion will not effect the main conclusions of this paper.

### 2.3 Stress path

Segura et al. (2011) model the influence of reservoir geometry and material properties on stress path using a more extensive suite of models considered in this paper. Using poroelastic constitutive material behaviour, Segura et al. (2011) observed that the stress arching effect is significant in small, thin reservoirs that are soft compared to the surrounding rock. Under such circumstances, the stresses will not evolve within the reservoir and so stress evolution occurs primarily in the overburden and sideburden. Furthermore, stiff reservoirs do not display any stress arching regardless of the geometry. Stress anisotropy decreases with reduction in bounding material strength (e.g., Young's modulus), and this is especially true for small reservoirs. However, when the dimensions extend in one or two lateral directions the reservoir deforms uniaxially and the horizontal stresses are controlled by the reservoir Poisson's ratio.

To understand the stress path parameters, it is helpful to review the concept of effective stress and the Mohr circle. The concept of stress path is based on Terzhagi (1943) effective stress principle and is expressed assuming compression is positive:

$$\sigma^e = \sigma - bP, \quad (7)$$

where  $\sigma^e$  is the effective stress,  $\sigma$  is the total stress,  $P$  is pressure, and  $b$  is Biot's coefficient (which we assume is 1 for simplicity in this paper). The Mohr circle is an effective graphical representation of the stress state for a material point (e.g., Jaeger et al. 2007). The Mohr circle allows one to evaluate how close a region is to elastic failure assuming the normal and shear strength is known. The Mohr circle is defined in terms of the principle stresses considering the



normal  $\sigma^e$ ) and the shear stresses ( $\tau$ ) on a plane at an angle  $\theta$ :

$$\sigma^e = \frac{\sigma_3^e + \sigma_1^e}{2} + \frac{\sigma_3^e - \sigma_1^e}{2} \cos \theta \quad (8)$$

$$\tau = \frac{\sigma_3^e - \sigma_1^e}{2} \sin \theta, \quad (9)$$

where  $\sigma_3^e$  and  $\sigma_1^e$  are the maximum and minimum principle stresses, respectively.

The stress path parameters describe the evolution of the Mohr circle and are defined by three terms, the stress arching parameter  $\gamma_3$ , the horizontal stress path parameter  $\gamma_1$  and the deviatoric stress path parameter or stress anisotropy parameter  $K$ . Since only two of the three parameters are independent we choose  $\gamma_3$  and  $K$  as the reference parameters (e.g., Segura et al. 2011). The stress arching parameter is defined

$$\gamma_3 = \frac{\Delta \sigma_3^e}{\Delta P} \quad (10)$$

and describes the development of stress arching, where  $\gamma_3$  high indicates stress arching is occurring with very little stress evolution in the reservoir. The stress anisotropy parameter is defined

$$K = \frac{\Delta \sigma_1^e}{\Delta \sigma_3^e} \quad (11)$$

and describes the development of stress anisotropy, where  $K$  low indicates increase in stress anisotropy with lower changes in horizontal effective stress with respect to changes in vertical effective stress.

### 3 Numerical examples

#### 3.1 Geomechanical model

Segura et al. (2011) generated a series of 3D numerically coupled poroelastic hydro-mechanical models to investigate the influence of reservoir geometry and material property contrast on the development of reservoir stress path. In their paper, they show the importance of reservoir geometry and material property discontinuities on the development of stress anisotropy. In this paper, we focus on a subset of those reservoir geometries (see Fig. 1) and extended the simulation to include plasticity. The three reservoir geometries are described by a rectilinear sandstone reservoir at depth of 3050 m and having vertical thickness of 76 m. To reduce the computational requirements, the model is reduced to one-quarter geometry based on symmetry arguments. A vertical production well is located in the centre of the reservoir (i.e., at the origin) and produces until the pore pressure declines to 10 MPa within

the reservoir. The surrounding volume is defined laterally 10 km  $\times$  10 km and vertically 3220 m, where the non-reservoir rock is shale. The lateral dimensions of the three reservoir geometries are:

- Small reservoir: lateral dimension 190.5 m  $\times$  190.5 m
- Elongate reservoir: lateral dimension 4000 m  $\times$  200 m
- Extensive reservoir: lateral dimension 4000 m  $\times$  4000 m

At reservoir depth, the strength of the overburden and reservoir is equivalent (see Segura et al. 2011) for discussion of geomechanical model parameters). Although ELFEN is capable of incorporating anisotropic elastic material within the geomechanical simulation, we limit the material elasticity to isotropy to allow a clear analysis of geometry related stress-induced anisotropy.

#### 3.2 Stress path evolution

Figure 2 plots the evolution of the stresses during production for several specified points in the reservoir: at the production well and at the edges of the reservoir (the locations of points 1, 2 and 3 can be seen in Fig. 3). The stress path parameters can be estimated from the slopes of these curves. The slope of the curves in the top panels represents the stress arching parameter  $\gamma_3$  and the slope of the curves in the bottom panels the stress anisotropy parameter  $K$ . The stress path development for both the stress arching and stress anisotropy parameters is linear for the small reservoir ( $K \approx 0.4$  and  $\gamma_3 \approx 0.3$ ). This stress path development is characteristic of elastic behaviour. However, the stress path development becomes progressively nonlinear for the elongate and extensive geometry, respectively. For the extensive reservoir, the evolution of the stress anisotropy is characteristic of uniaxial compaction (see Fig. 5 in Pouya et al. 1998). Initially, the stress anisotropy has an elastic phase (low  $K$ ) and then evolves asymptotically into another linear final trend. The transition occurs, while the material undergoes shear-enhanced compaction (stress state intersects the yield surface and plastic consolidation). The final linear trend depends on the plastic potential of the constitutive model (i.e., is a function of the strain hardening). The stress arching is initially low but increases as failure within the reservoir increases and sheds the load onto the side-burden. For the elongate reservoir, the asymmetry of the geometry leads to a behaviour differing from uniaxial compaction. The stress arching is relatively linear and high ( $\gamma_3 \approx 0.9$ ), yet the stress anisotropy transitions from high ( $K \approx 0.9$ ) to moderate ( $K \approx 0.4$ ).

The linear trends of these curves are shown in Table 1 along with the poroelastic predictions (see Segura et al. 2011). There are similarities between the poroelastic and

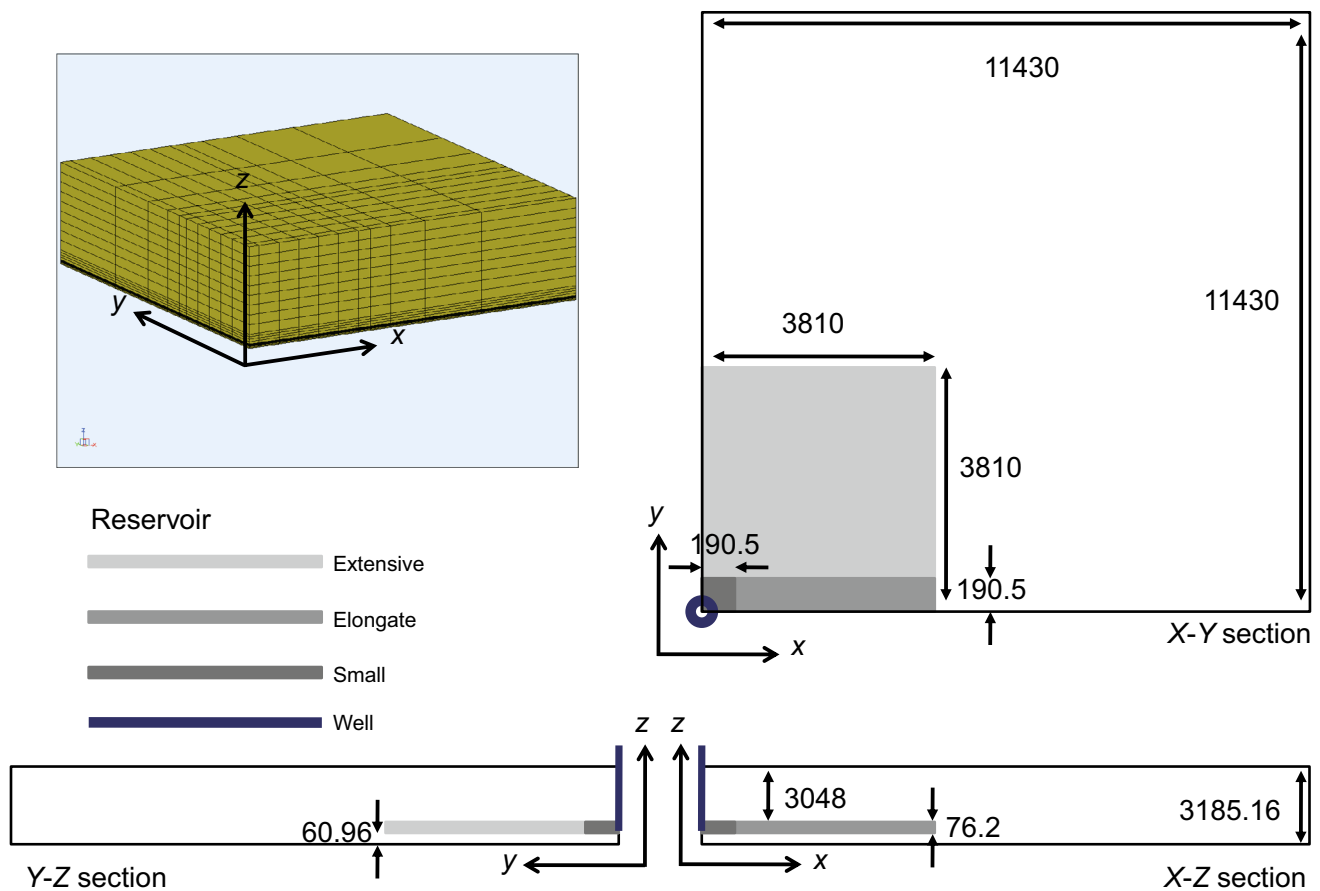


**Fig. 1** Geometry of the three simple reservoir models (all spatial units are in metres). The structured finite-element mesh used in the geomechanical simulation is illustrated *top-left*, and the locations of the three reservoir geometries are displayed in *X–Y (top-right)*, *X–Z (bottom-right)* and *Y–Z (bottom-left)* sections

poroelastoplastic case for the small geometry, with the exception of more moderate stress arching along the boundaries of the poroelastoplastic case. However, there are noticeable differences between the poroelastic and poroelastoplastic simulation results for the elongate and extensive geometries. The elongate geometry shows greater stress arching with similar moderate stress anisotropy (after the transition from high). The evolution of the stress parameters in the extensive model is more complicated (i.e., nonlinear). The stress arching evolves from low to moderate, whereas the stress anisotropy fluctuates from low to high and then moderate.

### 3.3 Seismic anisotropy

We use the modelled stress tensors at the end of production to compute the development of stress-induced *P*-wave anisotropy. To do so, we assume the initial crack densities ( $\varepsilon_i^0$ ) and initial aspect ratios ( $a_i^0$ ) are isotropic (e.g.,  $\varepsilon_x^0 = \varepsilon_y^0 = \varepsilon_z^0$ ) for simplicity. This could be relaxed if there

were prior petrophysical information to suggest otherwise; in real field examples this is likely to be the case (e.g., Crampin 2003). Following the calibration studies of Angus et al. (2009, 2011), we choose  $\varepsilon_i^0 = 0.25$  and  $a_i^0 = 0.001$  for the sandstone reservoir and  $\varepsilon_i^0 = 0.125$  and  $a_i^0 = 0.005$  for the surrounding shale. These values are taken as representative of the global trend for sandstones and shales observed by Angus et al. (2009, 2011). However, these measurements were biased towards rocks sampled from reservoir depths, with limited data from shallower cores (which are often of less interest commercially). For the extensive reservoir, stress changes are observed to occur as a result of production throughout the overburden even up to the surface. It is unclear whether the trends observed by Angus et al. (2009, 2011) are suitable for softer, poorly consolidated near-surface material. Thus, for the extensive reservoir geometry, an additional simulation is performed using the same initial crack densities, but scaling the initial aspect ratio with depth, with an aspect ratio of 0.001 at the base of the model and increasing to 0.01 at the surface.

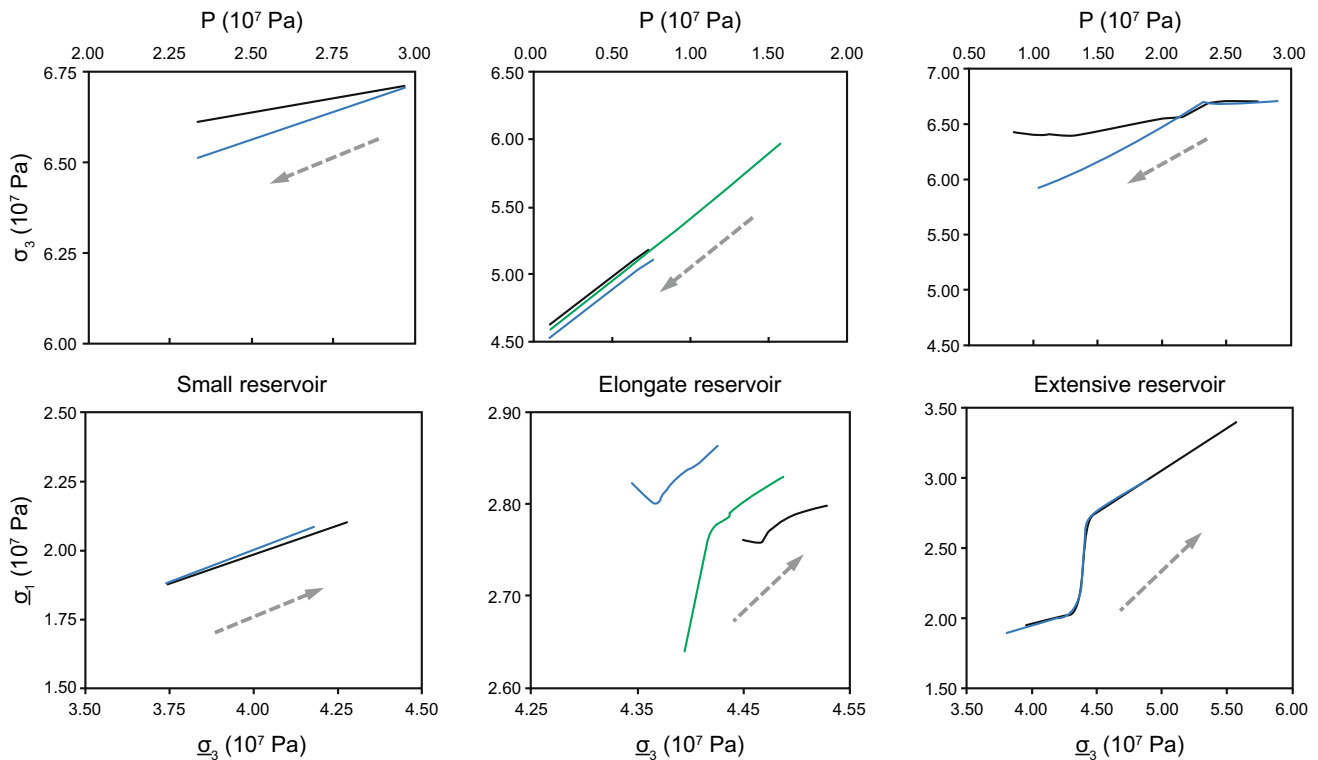


**Fig. 2** Evolution of stress path parameters for the three reservoir geometries: (*left column*) small reservoir, (*middle column*) elongate reservoir and (*right column*) extensive reservoir. The slope of the curves in *each panel* represents the stress path parameters: (*top row*) stress arching parameter 3 and (*bottom row*) stress anisotropy parameter  $K$ . The *solid lines* are colour-coded black for point 1, green for point 2 and blue for point 3. The *dashed arrow* represents the direction of evolution of the stress path parameter

This is done to replicate shallow core measurements of shale velocity stress dependence (e.g., Podio et al. 1968), where increasing the aspect ratio tends to reduce the overall stress dependence except at very low confining stresses.

### 3.4 Small reservoir geometry

The small reservoir geometry is characteristic of a highly compartmentalized reservoir, with limited spatial extent. The stress-induced anisotropy that develops during production is plotted in Figs. 3 and 4. These plots show the maximum  $P$ -wave anisotropy for near-vertical incidence waves ( $0^\circ$ – $30^\circ$ ), as well as upper hemisphere plots showing the  $P$ -wave velocity at all incidence angles for specified points in and around the reservoir. The  $P$ -wave anisotropy is confined to a small volume surrounding the sandstone reservoir with modelled  $P$ -wave anisotropy  $>1\%$ .

For points within the reservoir, we observe an approximately hexagonal anisotropic symmetry, where the maximum  $P$ -wave velocity is vertical. This implies that the reservoir is compacting vertically (closing of microcracks that are oriented horizontally, increasing vertical  $P$ -wave velocities). For points outside the reservoir, hexagonal symmetry is again observed, but the vertical  $P$ -wave

velocity is now the minimum velocity, implying vertical extension (opening of microcracks that are oriented horizontally, reducing vertical  $P$ -wave velocities).

However, there is in fact an observed reduction in both the  $P$ - and  $S$ -wave velocities throughout the reservoir on the order of 0.5 % or less. For point 1, the maximum  $P$ -wave velocity (which is vertical) is 1666 m/s, yet the initial isotropic pre-production  $P$ -wave velocity was 1672 m/s. Points 2 and 3 within the reservoir adjacent to the boundary also display sub-vertical maximum  $P$ -wave velocity, with minimum  $P$ -wave velocity oriented horizontally perpendicular to the reservoir edge. This implies that the maximum horizontal stress is parallel to the reservoir edge. For points 5 and 6, along the borehole above and below the reservoir, the post-production anisotropic symmetries predict minimum vertical velocities equal to the initial pre-production velocities and maximum sub-horizontal  $P$ -wave velocities larger than pre-production values.

Table 2 summarizes the anisotropic symmetry decomposition of the stress-induced anisotropy using the approach of Browaeys and Chevrot (2004). Although the stress-induced anisotropy is weak (i.e., isotropic components are all 99 %) for all grid points, there are components of the elastic tensor that require hexagonal and



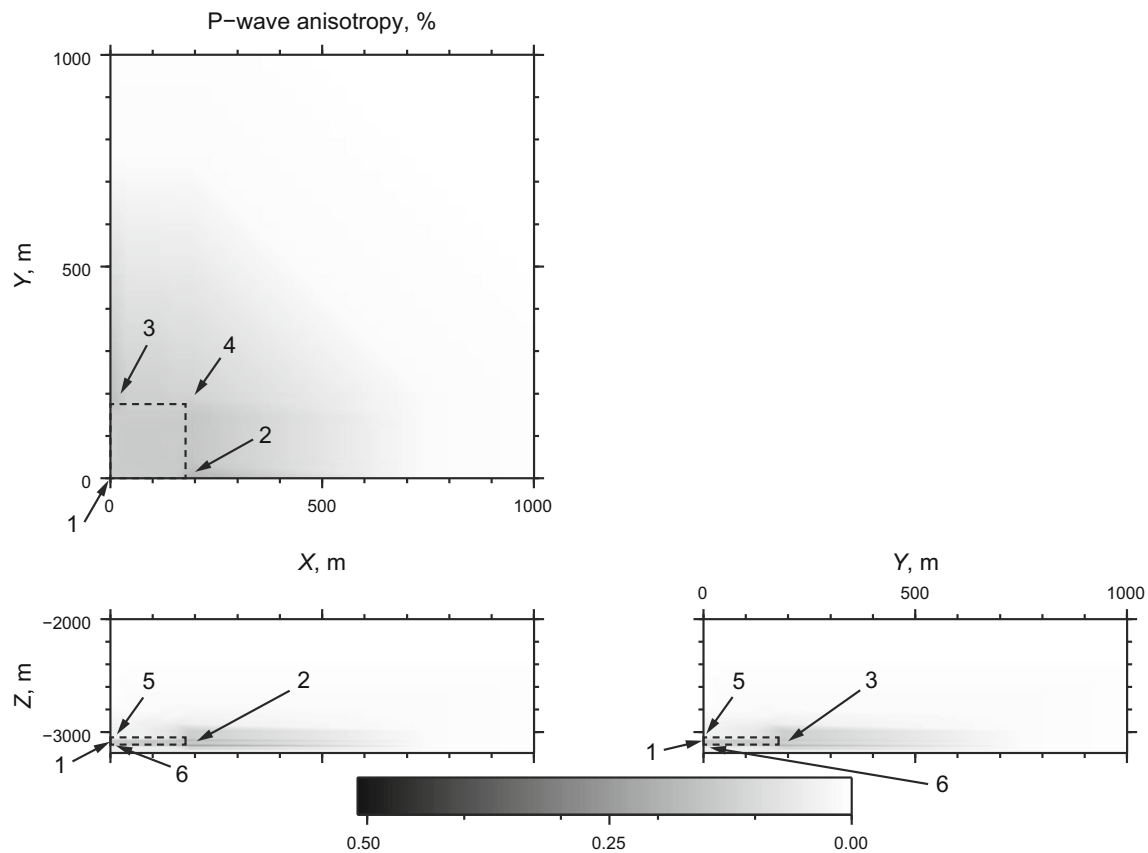


**Fig. 3** Contour plot of maximum *P*-wave anisotropy (%) for near offset seismic propagation ( $0^\circ$  to  $30^\circ$ ) for the small reservoir geometry. (In this and subsequent figures, the *x*-*z* section is at *y* = 0 m, the *y*-*z* section is at *x* = 0 m, and the *x*-*y* section is at *z* = −3000 m. The reservoir is defined as the region within the *dashed lines*)

**Table 1** Stress parameters for poroelastic and poroelastoplastic geomechanical simulations. Note that the values for the extensive reservoir are estimated from the initial and final stage and so neglect the nonlinear stress path seen in Fig. 2

Model	Poroelastic			Poroelastoplastic		
	Point	<i>K</i>	$\gamma_3$	Point	<i>K</i>	$\gamma_3$
Small	1	0.42	0.12	1	0.41	0.16
	2	0.47	0.18	2	0.46	0.31
	3	0.47	0.18	3	0.46	0.31
Elongate	1	0.35	0.10	1	<i>n to m</i>	0.88
	2	0.40	0.12	2	<i>h to m</i>	0.94
	3	0.40	0.12	3	<i>n to m</i>	0.88
Extensive	1	0.33	0.00	1	<i>l-h-m</i>	<i>n to l</i>
	2	0.37	0.07	2	<i>l-h-m</i>	<i>m to l</i>
	3	0.37	0.07	3	<i>l-h-m</i>	<i>m to l</i>

*n to m* refers to transition from negative to moderate, *h to m* from high to moderate, *m to l* from moderate to low and *l-h-m* transition from low to high and then moderate

orthorhombic symmetry and hence do not fit elliptical anisotropy. These results are not consistent with other studies that suggest that  $\Delta\epsilon = \Delta\delta$  (e.g., Fuck et al. 2010;

Herwanger and Horne 2009). Rasolofosaon (1998) suggests that the lowest order of stress-induced anisotropic symmetry can be at most elliptical anisotropy,  $\Delta\epsilon = \Delta\delta$ . However, this is only the case when considering third-order elasticity theory and assuming isotropic third-order elastic tensors (see Fuck and Tsvankin 2009). For the microstructural nonlinear formulation in this paper, we are not limited to elliptical anisotropy.

The results from the small geometry are counter-intuitive and are not consistent with model predictions from other simulations (e.g., Fuck et al. 2009; Herwanger and Horne 2009), where reservoir compaction results in an increase in seismic velocities within the reservoir, and reduction in velocities in the over- and under-burden. Although we would expect the weak reservoir sandstone to deform under the increased effective stress conditions due to pore pressure reduction, we observe instead stress arching occurring within the vicinity of the reservoir. Since the strength of the reservoir and surrounding shale is approximately equal, the shale acts to support deformation occurring within the reservoir. In terms of the rock physics model, the reduction in pore pressure leads to an increase

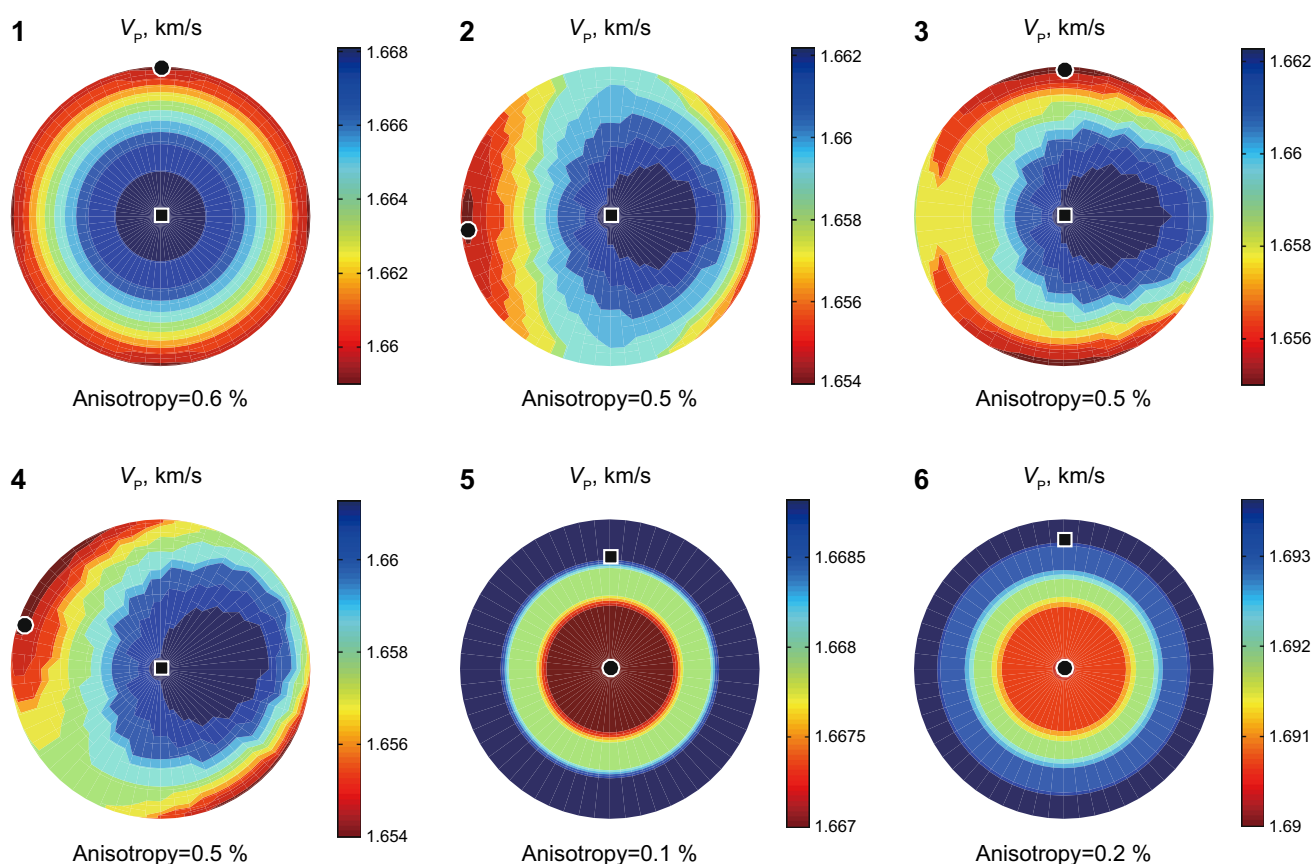


**Fig. 4** Upper-hemisphere plots of *P*-wave phase velocity for various points in the small reservoir geometry (see Fig. 3)

**Table 2** Decomposition of elastic tensor for all anisotropic symmetries for the small reservoir (labelled points shown in Fig. 3)

Point	Isotropic	Hexagonal	Tetragonal	Orthorhombic	Monoclinic	Triclinic
1	99.57	0.43	0.00	0.00	0.00	0.00
2	99.67	0.16	0.00	0.17	0.00	0.00
3	99.67	0.18	0.00	0.15	0.00	0.00
4	99.63	0.20	0.00	0.17	0.00	0.00
5	99.89	0.01	0.00	0.10	0.00	0.00
6	99.87	0.02	0.00	0.11	0.00	0.00

in microcracks (i.e., opening of existing cracks) with very little reservoir rock compaction and vertical extension above and below in the shale. The changes in seismic attributes suggest that most of the deformation is occurring inside and within the immediate vicinity of the reservoir with minimal influence on the surrounding shale. This is expected due to the small spatial dimensions of the reservoir, where the impact of pressure depletion limits the strength and spatial extend of stress redistribution.

### 3.5 Elongate reservoir geometry

For this geometry, the elongate reservoir is characteristic of a relatively large compartmentalized reservoir, such as a horst bounded by impermeable faults. In Figs. 5 and 6, the

*P*-wave anisotropy is no longer confined to a small volume immediately surrounding the sandstone reservoir, but extends laterally away from the long-axis (*y*-axis) of the reservoir by as much as 500 m. There is also a weak increase in *P*-wave anisotropy laterally away from the short-axis, and vertically towards the surface. The largest predicted anisotropy is as large as 3 % and mainly within the side-burden adjacent to the long-axis of the reservoir.

Focusing on the anisotropic symmetries, we observe noticeable differences from the small reservoir. For point 1, in the reservoir adjacent to the well, the maximum *P*-wave velocity is 1840 m/s and vertical, a decrease from the initial pre-production *P*-wave velocity of 1863 m/s similar to the small reservoir geometry. Points 2 and 4 within the reservoir adjacent to the short boundary display

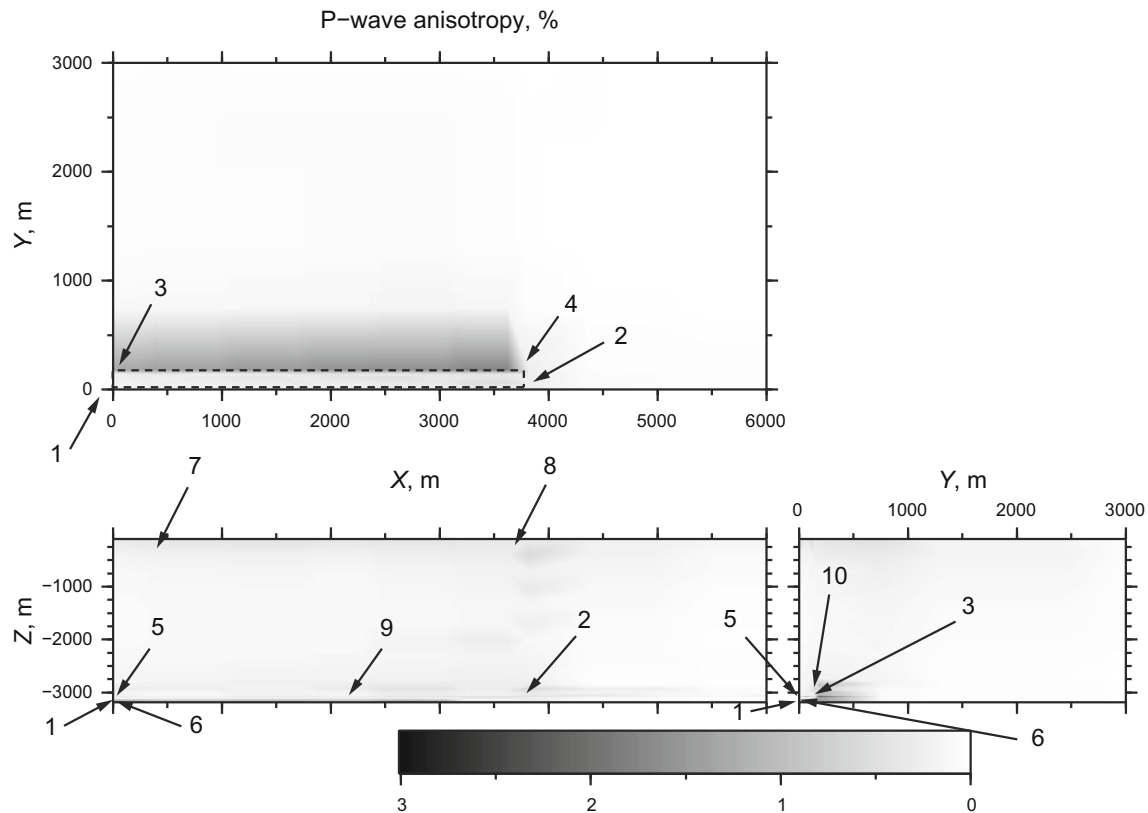


**Fig. 5** Contour plot of maximum *P*-wave anisotropy (%) for near offset seismic propagation ( $0^\circ$  to  $30^\circ$ ) for the elongate reservoir geometry

sub-horizontal maximum *P*-wave velocity (an increase of up to 4 m/s from pre-production) perpendicular to the long-axis, implying a preferred orientation of vertical microcracks oriented parallel to the reservoir short-axis. Point 3 within the reservoir along the long-axis shows sub-horizontal maximum *P*-wave velocity (an increase from pre-production) parallel to the long-axis. The post-production anisotropic symmetry for point 5 predicts maximum *P*-wave velocity slightly greater than pre-production (2 m/s) normal to the long-axis with microcracks oriented sub-vertically perpendicular to the *x*-axis. For point 6, the symmetry appears to be rotated by  $90^\circ$  about the vertical axis with horizontal maximum *P*-wave velocity parallel to the *x*-axis (an increase of approximately 20 m/s) with vertically oriented microcracks parallel to the long-axis. Points 7 and 8 in the near sub-surface indicate slight extension with the opening of horizontal microcracks (decrease of vertical velocity of 1 m/s) with a more prominent horizontal velocity increase (roughly 5 m/s) perpendicular to the long-axis. Points 9 and 10 represent regions adjacent to the reservoir in the overburden some distance from the borehole and show a sub-horizontal increase in velocity along the *y*-axis with microcracks oriented sub-horizontally. Table 3 summarizes the anisotropic symmetry decompositions for the elongate reservoir points.

These results are slightly more intuitive than those of the small geometry. In this model, we still see a velocity reduction near the well within the reservoir, but there is now compaction occurring along the edges of the reservoir, albeit horizontal and not vertical. Thus, we are still observing stress arching above the reservoir, but with some of the load “pushing” into the sides of the reservoir. The changes in seismic attributes suggest that the deformation is no longer confined to the immediate vicinity of the reservoir, where we are observing significant perturbations in the side-burden as well as near the surface.

### 3.6 Extensive reservoir geometry

The extensive reservoir geometry is characteristic of a non-compartmentalized reservoir. Figures 7 and 8 display the results of the modelled *P*-wave anisotropy based on using the un-scaled initial aspect ratio (i.e., the same rock physics model parameters as was used for the other reservoir geometries). The *P*-wave anisotropy is on the order of 25 % near the surface of the model and hence any anisotropy within the vicinity of the reservoir is overshadowed by the surface perturbations. The anisotropic symmetry for point 7 near the well displays characteristic subsidence pattern with extension vertically (i.e., horizontal microcrack development) and radial horizontal compression.

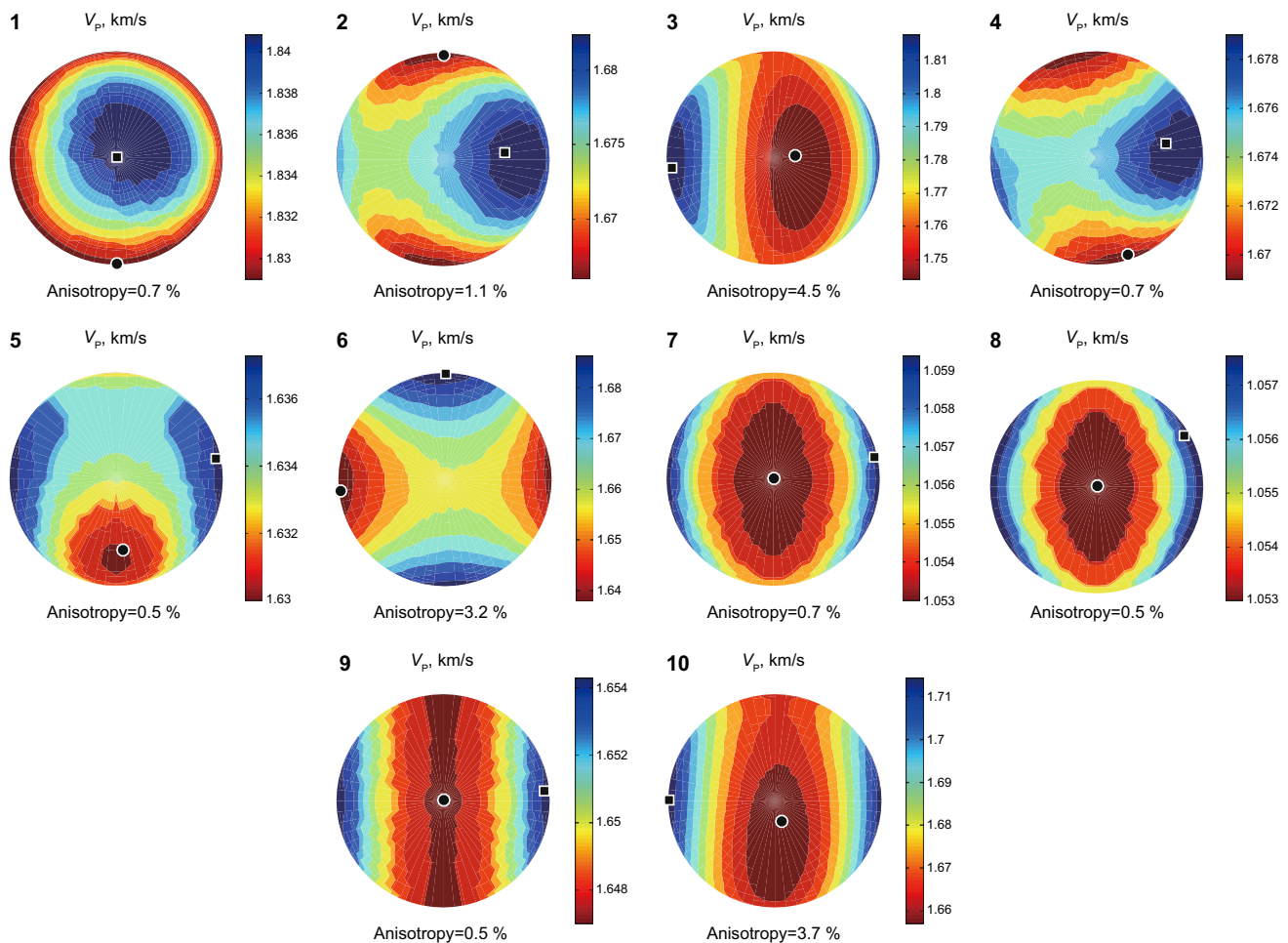


**Fig. 6** Upper-hemisphere plots of *P*-wave phase velocity for various points in the elongate reservoir geometry (see Fig. 5)

**Table 3** Decomposition of elastic tensor for all anisotropic symmetries for elongate reservoir (labelled points shown in Fig. 4)

Point	Isotropic	Hexagonal	Tetragonal	Orthorhombic	Monoclinic	Triclinic
1	99.45	0.53	0.00	0.01	0.01	0.00
2	99.27	0.37	0.00	0.36	0.00	0.00
3	96.75	2.43	0.00	0.82	0.00	0.00
4	99.51	0.25	0.00	0.24	0.00	0.00
5	99.74	0.13	0.00	0.13	0.00	0.00
6	97.83	1.21	0.00	0.96	0.00	0.00
7	99.49	0.34	0.00	0.17	0.00	0.00
8	99.58	0.24	0.00	0.18	0.00	0.00
9	99.60	0.35	0.00	0.01	0.04	0.00
10	97.23	2.38	0.00	0.39	0.00	0.00

Point 8 is near the edge of the subsiding region and displays sub-horizontal compression in the *y*-direction (or tangential to the subsidence bowl) with sub-vertical microcracks oriented along the *y*-axis (tangential to the subsidence bowl). This result is consistent with fast shear-wave polarization observations and predictions at Valhall (see Fig. 15 of Herwanger and Horne 2009).

Figures 9 and 10 show the results of the anisotropy predictions after defining a depth-dependent initial aspect ratio in order to focus in on perturbations within the vicinity of the reservoir. The results indicate that *P*-wave anisotropy is of the order of 2 % within the side-burden and over-burden. The volume of rock affected extends laterally away from the reservoir boundary by as much as

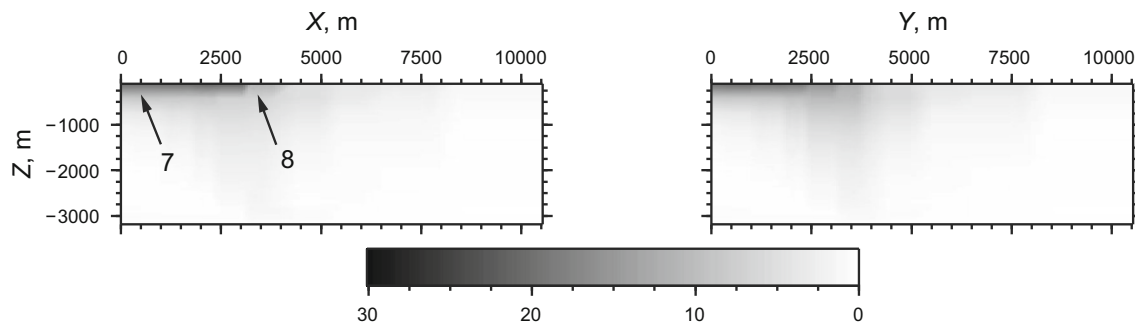


**Fig. 7** Contour plot of maximum  $P$ -wave anisotropy (%) for near offset seismic propagation ( $0^\circ$  to  $30^\circ$ ) for the extensive reservoir geometry for the  $x$ - $z$  section. The large magnitude of anisotropy reflects the sensitivity of the elastic model to the rock physics input parameters. In this case, the rock physics parameters are based on core taken from reservoir depths and so are not representative of near-surface rock

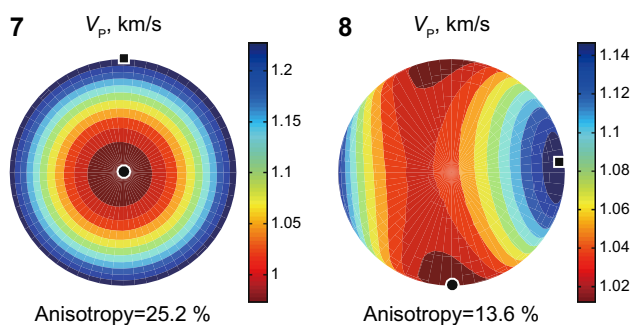


**Fig. 8** Upper-hemisphere plots of  $P$ -wave phase velocity for various points in the extensive reservoir geometry for the  $x$ - $z$  section (see Fig. 7)

1000 m. Looking at the anisotropic symmetries, we again observe noticeable differences from the other reservoir geometries. For point 1, the maximum  $P$ -wave velocity is 1685 m/s and vertical, yet the initial isotropic pre-production  $P$ -wave velocity is 1695 m/s. Points 2 and 3 within the reservoir adjacent to the boundaries display sub-horizontal maximum  $P$ -wave velocity (increase of up to 5 m/s from pre-production) parallel to the boundary, and with a preferred orientation of vertical microcracks oriented parallel to the reservoir edge. Point 4 at the corner of the reservoir indicates sub-horizontal maximum  $P$ -wave velocity (greater than the pre-production isotropic velocity) skirting around the reservoir edge with sub-vertical microcracks oriented tangential to the boundary. The post-production anisotropic symmetry for point 5 indicates extension in the overburden, with maximum  $P$ -wave velocity vertical and slightly less than pre-production (5 m/s), and microcracks oriented vertically and radial. For point 6, the symmetry is VTI maximum  $P$ -wave velocity horizontal (increase of approximately 15 m/s) with horizontally oriented microcracks. Table 4 summarizes the anisotropic symmetry decomposition of the stress-induced anisotropy.

In the near surface, these results are consistent with Herwanger and Horne (2009) and Fuck et al. (2010). However, differences can be seen within the vicinity of the reservoir, where the influence of reservoir geometry and the poroelastoplastic constitutive model impacts the development of stress arching.

#### 4 Discussion

The results of the rectilinear reservoir model show that the geometry of the reservoir influences stress path evolution during production, and therefore evolution of seismic anisotropy. For the small reservoir, the geomechanical stress anisotropy is moderate reflecting the influence of the reservoir boundaries on stress redistribution. Yet the developed seismic anisotropy is low due to the limited volumetric influence of the small reservoir as well as the weak development of stress arching in the side-burden. Under such circumstances, it would be reasonable to expect little or no microseismicity. For the extensive reservoir, the geomechanical stress and seismic anisotropy are high resulting from the large size of influence of the producing reservoir. However, the reservoir experiences significant shear-enhanced compaction during production, indicating that the time evolution of anisotropy is necessary for the characterization of compacting reservoirs. There would likely be significant microseismicity occurring within the side-burden due to stress arching leading to larger zones of high shear stress and failure. Also, due to the significant stress redistribution from fluid extraction, microseismicity would likely be observed within the shallow subsurface. This will have important implications for assessing the risk of compaction on production related activities, from the surface down to the reservoir. The elongate reservoir displays the greatest asymmetry, with significant seismic anisotropy (and hence strong potential for shear type



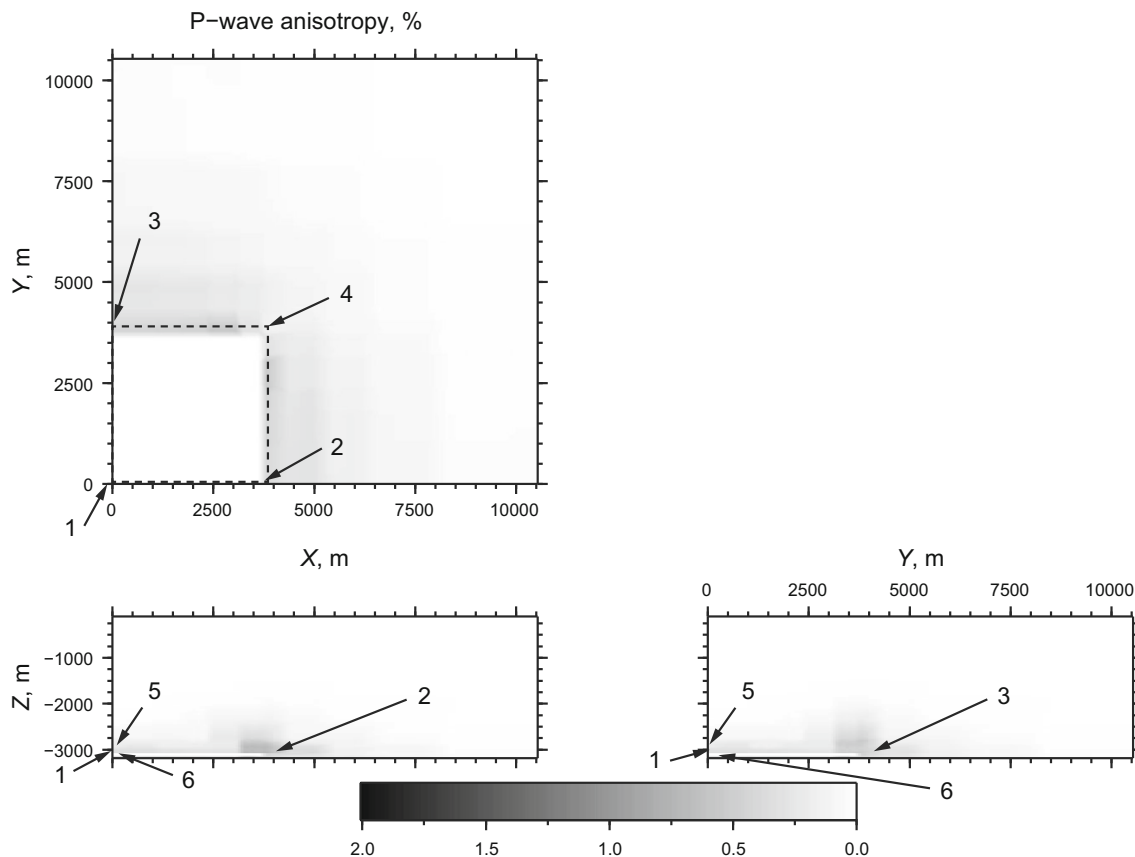


**Fig. 9** Contour plot of maximum *P*-wave anisotropy (in percent) for near offset seismic propagation ( $0^\circ$  to  $30^\circ$ ) for the extensive reservoir geometry after applying an ad hoc depth-dependent scaling of the nonlinear rock physics input parameters

microseismicity) developing along the long-edge of the reservoir. Although the reservoir experiences shear-enhanced compaction within the reservoir, stress arching remains relatively high and suggests that stress arching could have significant influence the fault/fluid-flow behaviour.

In all simulations, it has been shown that elliptical anisotropy is not a prerequisite of stress-induced anisotropy and is controlled not only by model geometry but also the rock physics model used. However, there is no unambiguous diagnostic link between predicted seismic anisotropy and stress path parameters. The most crucial point to note is the dependence of the seismic predictions on the rock physics model to map geomechanical parameters to dynamic elasticity. In particular, the depth dependence of the rock physics model is poorly constrained, which can lead to biases in predicted magnitude of seismic anisotropy. However, in full field simulations the models can be calibrated via history matching (e.g., Kristiansen and Plischke 2010). Certainly a parametric study of seismic attributes to the stress sensitivity of nonlinear rock physics models would be useful to determine the most influential model input parameters.

Nevertheless, this paper demonstrates that detectable amounts of seismic anisotropy can be produced by stress changes in and around a producing reservoir. At present there is a push towards developing methods to image-induced geomechanical deformation (e.g., Verdon et al. 2011; He et al. 2016a; Angus et al. 2015). Normal incidence travel-time shifts characterized by “R-factors” (e.g., Hatchell and Bourne 2005; He et al. 2016b) have been the most common observation used to do so. However, R-factors do not provide a full characterization of the changes in triaxial state, nor do all modes of geomechanical deformation lead to normal incidence travel-time shifts (for example changes in horizontal stresses). Therefore, characterization of seismic anisotropy in and around a producing reservoir can provide a more complete picture of deformation. This paper has outlined a workflow for predicting seismic anisotropy based on geomechanical simulation. By imaging seismic anisotropy around deforming reservoirs, we can begin to match modelled predictions with field observations in order to improve our understanding of production-induced deformation.

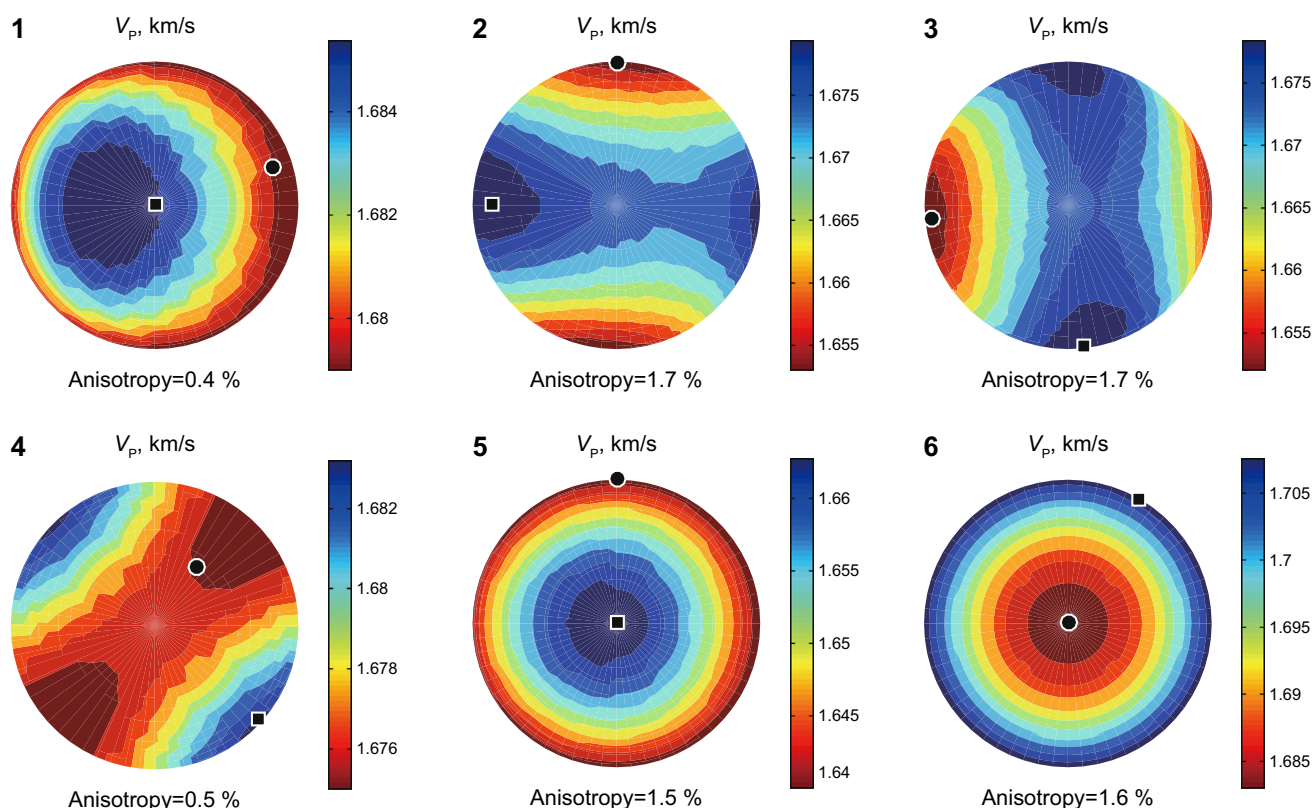


**Fig. 10** Upper-hemisphere plots of P-wave phase velocity for various points in the extensive reservoir geometry (see Fig. 9)

**Table 4** Decomposition of elastic tensor for all anisotropic symmetries for extensive reservoir (labelled points in Figs. 5, 6)

Point	Isotropic	Hexagonal	Tetragonal	Orthorhombic	Monoclinic	Triclinic
1	99.62	0.34	0.00	0.04	0.00	0.00
2	98.79	0.35	0.00	0.86	0.00	0.00
3	98.79	0.28	0.00	0.93	0.00	0.00
4	99.59	0.34	0.00	0.03	0.04	0.00
5	98.87	1.07	0.00	0.00	0.06	0.00
6	98.77	0.17	0.00	1.06	0.00	0.00
7	81.39	2.56	0.06	15.99	0.00	0.00
8	89.89	8.58	0.00	1.53	0.00	0.00

## 5 Conclusions

In this paper, we present a workflow that links coupled fluid-flow and geomechanical simulation with seismic modelling. The workflow allows the prediction of seismic anisotropy induced by non-hydrostatic stress changes. The seismic models from the coupled flow-geomechanical simulations for several rectilinear reservoir geometries highlight the relationship between reservoir geometry, stress path and seismic anisotropy. The results confirm that reservoir geometry influences the evolution of stress during production and subsequently stress-induced seismic anisotropy. Although the geomechanical stress anisotropy is high for the small reservoir, the effect of stress arching and

the ability of the side-burden to support the excess load limit the overall change in effective stress resulting in minimal development of seismic anisotropy. For the extensive reservoir, stress anisotropy and induced seismic anisotropy are high. The extensive and elongate reservoirs experience significant shear-enhanced compaction, where the inefficiency of the developed stress arching in the side-burden cannot support the excess load. The elongate reservoir displays significant stress asymmetry, with seismic anisotropy developing predominantly along the long-edge of the reservoir. Although the link between stress path parameters and seismic anisotropy is complex, the results suggest that developments in time-lapse seismic anisotropy analysis will have potential in calibrating geomechanical

models. Furthermore, the results of the seismic anisotropy analysis find that elliptical anisotropy is not a prerequisite of stress-induced anisotropy, where the anisotropic symmetry is controlled not only by model geometry but also the nonlinear rock physics model used.

**Acknowledgements** The authors would like to thank Rockfield Software and Roxar for permission to use their software. We also acknowledge ITF and the sponsors of the IPEGG project, BG, BP, Statoil and ENI. D.A. Angus also acknowledges the Research Council UK (EP/K035878/1; EP/K021869/1; NE/L000423/1) for financial support.

**Open Access** This article is distributed under the terms of the Creative Commons Attribution 4.0 International License (<http://creativecommons.org/licenses/by/4.0/>), which permits unrestricted use, distribution, and reproduction in any medium, provided you give appropriate credit to the original author(s) and the source, provide a link to the Creative Commons license, and indicate if changes were made.

## References

- Alassi H, Holt R, Landro M. Relating 4D seismics to reservoir geomechanical changes using a discrete element approach. *Geophys Prospect*. 2010;58:657–68.
- Angus DA, Verdon JP, Fisher QJ, Kendall J-M. Exploring trends in microcrack properties of sedimentary rocks: an audit of dry-core velocity-stress measurements. *Geophysics*. 2009;74:E193–203.
- Angus DA, Kendall J-M, Fisher QJ, Segura JM, Skachkov S, Crook AJL, Dutko M. Modelling microseismicity of a producing reservoir from coupled fluid-flow and geomechanical simulation. *Geophys Prospect*. 2010;58:901–14.
- Angus DA, Verdon JP, Fisher QJ, Kendall J-M, Segura JM, Kristiansen TG, Crook AJL, Skachkov S, Yu J, Dutko M. Integrated fluid-flow, geomechanic and seismic modelling for reservoir characterization. *Can Soc Explor Geophys Rec*. 2011;36(4):18–27.
- Angus DA, Verdon JP, Fisher QJ. Exploring trends in microcrack properties of sedimentary rocks: an audit of dry and water saturated sandstone core velocity stress measurements. *Int J Geosci Adv Seismic Geophys*. 2012;3:822–33.
- Angus DA, Dutko M, Kristiansen TG, Fisher QJ, Kendall J-M, Baird AF, Verdon JP, Barkved OI, Yu J, Zhao S. Integrated hydro-mechanical and seismic modelling of the Valhall reservoir: a case study of predicting subsidence, AVOA and microseismicity. *Geomech Energy Environ*. 2015;2:32–44.
- Aziz K, Settari A. *Petroleum reservoir simulation*. London: Applied Science Publishers Ltd.; 1979.
- Baird AF, Kendall J-M, Angus DA. Frequency dependent seismic anisotropy due to fracture: fluid flow versus scattering. *Geophysics*. 2013;78(2):WA111–22.
- Browaeys JT, Chevrot S. Decomposition of the elastic tensor and geophysical applications. *Geophys J Int*. 2004;159:667–78.
- Brown RJS, Korringa J. On the dependence of the elastic properties of a porous rock on the compressibility of the pore fluid. *Geophysics*. 1975;40:608–16.
- Chapman M. Frequency-dependent anisotropy due to meso-scale fractures in the presence of equant porosity. *Geophys Prospect*. 2003;51:369–79.
- Crampin S. The new geophysics: shear-wave splitting provides a window into the crack-critical rock mass. *Lead Edge*. 2003;22(6):536–49.
- Crook AJL, Yu J-G, Willson SM. Development and verification of an orthotropic 3-D elastoplastic material model for assessing borehole stability. In: *shales: SPE/ISRM Rock Mechanics Conference*. Texas: Irving; 2002, 20–23 Oct, p. 78239.
- Crook AJL, Willson SM, Yu J-G, Owen DRJ. Predictive modelling of structure evolution in sandbox experiments. *J Struct Geol*. 2006;28:729–44.
- Dean RH, Gai X, Stone CM, Minkoff SE. A comparison of techniques for coupling porous flow and geomechanics. *SPE*. 2003;79709:1–9.
- Dewhurst DN, Siggins AF. Impact of fabric, microcracks and stress field on shale anisotropy. *Geophys J Int*. 2006;165:135–48.
- Fuck RF, Tsvankin I. Analysis of the symmetry of a stressed medium using nonlinear elasticity. *Geophysics*. 2009;74(5):WB79–87.
- Fuck RF, Bakulin A, Tsvankin I. Theory of traveltimes shifts around compacting reservoirs: 3D solutions for heterogeneous anisotropic media. *Geophysics*. 2009;74(1):D25–36.
- Fuck RF, Tsvankin I, Bakulin A. Influence of background heterogeneity on traveltimes shifts for compacting reservoirs. *Geophys Prospect*. 2010;59(1):78–89.
- Geertsma J. Land subsidence above compacting oil and gas reservoirs. *J Pet Geol*. 1973;25(6):734–44.
- Hall SA, Kendall J-M, Maddock J, Fisher Q. Crack density tensor inversion for analysis of changes in rock frame architecture. *Geophys J Int*. 2008;173:577–92.
- Hatchell PJ, Bourne S. Rocks under strain: strain-induced time-lapse time shifts are observed for depleting reservoirs. *Lead Edge*. 2005;24:1222–5.
- He Y, Angus DA, Yuan S, Xu YG. Feasibility of time-lapse AVO and AVOA analysis to monitor compaction-induced seismic anisotropy. *J Appl Geophys*. 2015;122:134–48.
- He Y, Angus DA, Blanchard TD, Garcia A. Time-lapse seismic waveform modeling and seismic attribute analysis using hydro-mechanical models for a deep reservoir undergoing depletion. *Geophys J Int*. 2016a;205:389–407.
- He Y, Angus DA, Clark RA, Hildyard MW. Analysis of time-lapse travel-time and amplitude changes to assess reservoir compartmentalisation. *Geophys Prospect*. 2016b;64:54–67.
- Helbig K, Rasolofosaon PNJ. A theoretical paradigm for describing hysteresis and nonlinear elasticity in arbitrary anisotropic rocks. In: *Anisotropy 2000: fractures, converted waves and case studies 2000*.
- Herwanger J, Horne S. Linking reservoir geomechanics and time—lapse seismics: predicting anisotropic velocity changes and seismic attributes. *Geophysics*. 2009;74(4):W13–33.
- Herwanger JV, Schjøtt CR, Frederiksen R, If F, Vejbæk OV, Wold R, Hansen HJ, Palmer E, Koutsabeloulis N. Applying time-lapse seismic to reservoir management and field development planning at South Arne, Danish North Sea. In: *Vining BA, Pickering SC (eds) Petroleum geology: from mature Basins to New Frontiers, Proceedings of the 7th Petroleum Geology Conference*; 2010.
- Jaeger JC, Cook NGW, Zimmerman RW. *Fundamentals of rock mechanics*. 4th ed. Oxford: Blackwell Publishing; 2007.
- Johnson PA, Rasolofosaon PNJ. Manifestation of nonlinear elasticity in rock: convincing evidence over large frequency and strain intervals from laboratory studies. *Nonlinear Processes in Geophysics*. 1996;3:77–88.
- Kendall J-M, Fisher QJ, CoveyCrump S, Maddock J, Carter A, Hall SA, Wookey J, Valcke SLA, Casey M, Lloyd G, Ben Ismail W. Seismic anisotropy as an indicator of reservoir quality in siliciclastic rocks, structurally complex reservoirs. In: *Jolley SJ, Barr D, Walsh JJ, Knipe RJ, editors. Geological society. London: Special Publication; 2007. pp. 123–36*.
- Kristiansen TG, Plischke B. History matched full field geomechanics model of the Valhall Field including water weakening and repressurization. *SPE*. 2010;131505.

- Maultzsch S, Chapman M, Liu E, Li X-Y. Modelling frequency-dependent seismic anisotropy in fluid-saturated rock with aligned fractures: implication of fracture size estimation from anisotropic measurements. *Geophys Prospect*. 2003;51(5):381–92.
- Minkoff SE, Stone CM, Bryant S, Peszynska M, Wheeler MF. Coupled fluid flow and geomechanical deformation modeling. *J Pet Sci Eng*. 2003;38:37–56.
- Muntz S, Fisher QJ, Angus DA, Dutko M, Kendall JM. A project on the coupling of fluid flow and geomechanics. In: 9th US National Congress on Computational Mechanics, San Francisco, 2007, 23–26 July.
- Nur A, Simmons G. Stress-induced velocity anisotropy in rock: an experimental study. *J Geophys Res*. 1969;74:6667–74.
- Olofsson B, Probert T, Kommedal JH, Barkved OI. Azimuthal anisotropy from the Valhall 4C 3D survey. *Lead Edge*. 2003;22:1228–35.
- Olsen C, Christensen HF, Fabricius IL. Static and dynamic Young's moduli of chalk from the North Sea. *Geophysics*. 2008;73:E41–50.
- Podio AL, Gregory AR, Gray KE. Dynamic properties of dry and water-saturated Green River shale under stress. *SPE*. 1968;8(4):389–404.
- Pouya A, Djeran-Maigre I, Lamoureux-Var V, Grunberger D. Mechanical behaviour of fine grained sediments: experimental compaction and three-dimensional constitutive model. *Mar Pet Geol*. 1998;15:129–43.
- Prioul R, Bakulin A, Bakulin V. Nonlinear rock physics model for estimation of 3D subsurface stress in anisotropic formations: theory and laboratory verification. *Geophysics*. 2004;69:415–25.
- Rasolofosaon P. Stress-induced seismic anisotropy revisited. *Revue de l'institut français du pet*. 1998;53(5):679–92.
- Rutqvist J, Wu Y-S, Tsang CF, Bodvarsson G. A modeling approach for analysis of coupled multiphase fluid flow heat transfer, and deformation in fractured porous rock. *Int J Rock Mech Min Sci*. 2002;39:429–42.
- Sayers CM. Stress-dependent elastic anisotropy of sandstones. *Geophys Prospect*. 2002;50:85–95.
- Sayers CM. Asymmetry in the time-lapse seismic response to injection and depletion. *Geophys Prospect*. 2007;55(5):699–705.
- Sayers C, Kachanov M. Microcrack-induced elastic wave anisotropy of brittle rocks. *J Geophys Res*. 1995;100:4149–56.
- Schoenberg M, Sayers CM. Seismic anisotropy of fractured rock. *Geophysics*. 1995;60(1):204–11.
- Segura JM, Fisher QJ, Crook AJL, Dutko M, Yu J, Skachkov S, Angus DA, Verdon J, Kendall J-M. Reservoir stress path characterization and its implications for fluid-flow production simulations. *Pet Geosci*. 2011;17:335–44.
- Terzhagi K. Theoretical soil mechanics. New York: Wiley; 1943.
- Tod SR. The effects of stress and fluid pressure on the anisotropy of interconnected cracks. *Geophys J Int*. 2002;149:149–56.
- Verdon JP, Angus DA, Kendall J-M, Hall SA. The effects of microstructure and nonlinear stress on anisotropic seismic velocities. *Geophysics*. 2008;73(4):D41–51.
- Verdon JP, Kendall J-M, White DJ, Angus DA. Linking microseismic event observations with geomechanical models to minimise the risks of storing CO<sub>2</sub> in geological formations. *Earth Planet Sci Lett*. 2011;305:143–52.